PAPER

Synthesis, optical and ionic conductivity studies of a lithium cobalt germanate compound

Sourour Ben Yahya, [ID] *[a] Regis Barillé[b] and Bassem Louati[a]

A lithium cobalt germanate compound (Li_2CoGeO_4) was synthesized and studied. The X-ray powder diffraction pattern demonstrated a monoclinic crystal system with the *Pn* space group. The morphology and composition were done by scanning transmission electron microscopy and energy dispersive X-ray spectroscopy (SEM-EDS). A vibrational study confirmed the existence of the anion $(GeO_4)^{4-}$ and its vibrations. The estimated value of the direct band gap (E_g) was evaluated at 3.45 eV. The measurements of the electrical properties were performed in the frequency interval from 100 Hz to 1 MHz and the temperature range from 553 K to 663 K. The Nyquist plots revealed the existence of a single semicircle in all impedance spectra due to the grain interior effect. The AC electrical conduction in Li_2CoGeO_4 has been explained through several processes, which can be coupled with two different formalisms. The complex electric modulus studies $M^*(\omega)$ confirmed that the relaxation process is thermally activated.

1. Introduction

Germanium-based ceramic materials with the A_2MGeO_4 (A = K, Li, Na, Cs, Rb, … and M = Zn, Co, Mg, Mn, …) chemical formula have obtained growing attention, principally due to their interesting physical applications such as magnetic, catalytic, solid electrolytic properties for batteries, optics and photocatalysts.[1–5] A lot of research has been done on orthogermanate compounds with the formula A_2MGeO_4 (A = Li, Na and M = Zn, Co, Fe, Mn) and confirmed that this material is a potential cathode due to its high conductivity,[4] taking into account that the ionic conductivity is highly related to the structural rearrangement. The conductivity of this type of compound has been studied since the 1960s with different lithium and sodium environments, revealing that these materials can offer an almost perfect conductivity.[6] The LISICON compound, $Li_{3.5}Zn_{0.25}GeO_4$, presented an ionic conductivity higher than 10^{-1} S cm^{-1} at 673 K.[7] Moreover, the Ag_2ZnGeO_4 compound is an electronic semiconductor with σ $(60°) = 1 \times 10^{-2}$ (Ω cm)$^{-1}$.[8] S. Ben Yahya and B. Louati have studied the electric properties of A_2ZnGeO_4 (A = Li and K) compounds.[9,10] They have determined the electrical conductivity of these materials and estimated them: 10^{-3} (Ω m)$^{-1}$ and 10^{-5} (Ω m)$^{-1}$ for K_2ZnGeO_4 and Li_2ZnGeO_4 respectively. In this work Li_2CoGeO_4 (LCG) is studied. This material belongs to the same family of Li_2CoSiO_4 (LCS) with a structure derived from Li_3PO_4. Recently, the crystal structure, synthesis, and electrochemical properties of Li_2CoSiO_4 were widely examined for lithium ion

battery applications.[11–14] The goal of this work is to study the structure of Li_2CoGeO_4 synthetized by a traditional high temperature solid state method, in order to determine microstructure morphologies, crystal chemical characteristics and optical properties. In order to better understand the electric properties as electron and hole transport properties in this solid electrolyte compound, infrared analysis, X-ray diffraction and impedance spectroscopy were used for Li_2CoGeO_4 cathode materials in future lithium-ion batteries.

2. Experimental

2.1. Synthesis

The Li_2CoGeO_4 (LCG) material was prepared by a traditional high temperature solid state method and consists of heating several solids which react to form the required product. The mixed lithium cobalt germanate (Li_2CoGeO_4) was synthesized in a powder state from starting materials (Li_2CO_3, Co_3O_4 and GeO_2) with a high purity (Sigma-Aldrich, 99%) by heating stoichiometric quantities of the starting materials according to the following reaction:

The homogeneity of the beginning materials was finalized in the agate mortar and progressively dried up to 673 K for 15 h to avoid ambient humidity and gases, particularly CO_2 evaporation. The obtained black powder was ground again for 8 h and pressed into 8 mm pellets in diameter and 1 mm in thick using a 3 ton per cm^2 uniaxial pressure and sintered at 1123 K for 15 h to make the blue (LCG) compound.

2.2. Apparatus

The X-ray powder diffraction (XRD) pattern of prepared ceramic samples was done at room temperature using a monochromatic

[a]Laboratory of Spectroscopic Characterisation and Optics of Materials, Faculty of Sciences, University of Sfax, B. P. 1171, 3000 Sfax, Tunisia. E-mail: sourourbenyahia09@gmail.com

[b]Univ Angers, CNRS, MOLTECH-ANJOU, SFR MATRIX, F-49000 Angers, France

$$6Li_2CO_3 + 6GeO_2 + 2Co_3O_4 \longrightarrow 6Li_2CoGeO_4 + 6CO_2 + O_2 \qquad (1)$$

Cu-Kα radiation ($\lambda_{k\alpha} = 1.5406$ Å) in a wide range of Bragg angles from 10° to 60°. The crystal structure refinement was performed by the Rietveld analysis[15] of the X-ray powder diffraction documents *via* the FULLPROF software.[16] The morphology was investigated by EVO LS10 (Zeiss) scanning electron microscopy equipped with 0 energy-dispersive system: INCA-X (Oxford Instruments). The IR spectroscopic analysis was realized with an "FT-IR PerkinElmer" spectrometer in a wide range of wavenumber from 400 cm^{-1} to 1400 cm^{-1}. The optical properties of the Li$_2$CoGeO$_4$ were measured at room temperature using a UV-3101PC scanning spectrophotometer in a broad range of wavelengths from 200 nm to 800 nm. The electrical measurements of this material in a pellet form are thoroughly analyzed and studied in the frequency range between 40 Hz and 1 MHz and in a temperature range between 553 K and 663 K using a complex impedance analysis. The measurements are comprehensively discussed based on a number of theoretical models.

3. Results and discussion

3.1. X-ray diffractions analysis

The solid-state LCG is studied by powder X-ray diffraction for the analysis of the crystal structure. The Fig. 1 shows the experimental and calculated XRD profile of Li$_2$CoGeO$_4$ compounds. The Rietveld refinement of LCG samples was done

to collect the detailed crystal structure information with the unique crystallographic data of LCG as the first model. It is clear that no secondary phase and no impurity peak was detected which confirms the pure and good quality of the sample. The crystal structure of Li$_2$ZnGeO$_4$ is taken as an initial model and the starting positions of all atoms were first considered by analogy to the structure of this compound. A refinement is then done which converged swiftly to reasonable and reliable factors. The best refinement of the experimental profile is carried out by the monoclinic system with the *Pn* space group. The quality factor confirms the concurrence between the calculated and the observed profiles is $\chi^2 = 1.79$. The refined lattice parameters are $a = 6.369(2)$ Å, $b = 5.461(2)$ Å, $c = 5.006(1)$ Å, $\beta(°) = 90.10(0)$ and $V = 174.113(1)$ Å^3. They are in good agreement with the results of a LCG compound synthesized by the hydrothermal method. The Table 1 summarizes the refined crystallographic parameters of the Li$_2$CoGeO$_4$ compound. The atomic positions are listed in the Table 2 whereas the distances and bond angles are given in Table 3.

3.2. Description of crystal structure

Li$_2$BGeO$_4$ (B = Zn, Mn, Co) is categorized among the C-type compounds. It crystallized in the three-dimensional (3D) frameworks of the CoO$_4$ and GeO$_4$ tetrahedral units. The powder structure of Li$_2$CoGeO$_4$ indicates that it is isostructural like the Li$_2$ZnGeO$_4$ structure.[9] The framework structure of Li$_2$CoGeO$_4$ host can be considered as a Wurtzite structure with corner-sharing alternating between the corners of the GeO$_4$ and ZnO$_4$ tetrahedra. In general, the orthogermanates are characterized by tetrahedral anion units, in particular (GeO$_4$)^4,
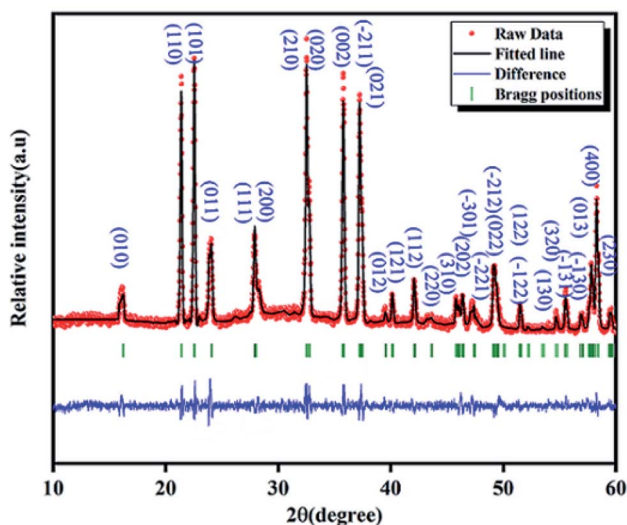

Fig. 1 Refined powder X-ray diffraction pattern for solide-state LCG, at room temperature: calculated data (black solid line), observed data (red)and the Bragg positions are observable by vertical bar.

Table 1 Rietveld refinement and crystal data of LCG matrix

Formula	Li$_2$CoGeO$_4$
Crystal system	Monoclinic
Space group	*Pn*
Unit lattice parameters (Å)	$a = 6.369(2)$
	$b = 5.461(2)$
	$c = 5.006(1)$
	$\beta(°) = 90.10(0)$
Unit cell volume (Å^3)	$V = 174.113(1)$
Z	2
R_p (%)	19.9
R_{wp} (%)	16.9
R_{exp} (%)	12.61
R_B (%)	3.31
R_F (%)	2.89
χ^2	1.79
ρ (g cm^{-3})	3.99

Table 2 The atomic coordinates of the compound Li_2CoGeO_4

Atom	Wyck	x	y	z	O_{cc}
Co	2a	0.31648	0.32427	0.50740	1
Ge	2a	0.06116	0.15955	0.00645	1
Li(1)	2a	0.52714	0.19827	0.00513	1
Li(2)	2a	0.82442	0.36037	0.48347	1
O(1)	2a	0.54090	0.16070	0.36206	1
O(2)	2a	0.33185	0.66021	0.43302	1
O(3)	2a	1.07739	0.17905	0.36900	1
O(4)	2a	0.30757	0.32104	0.88830	1

Table 3 Selected distances of Li_2CoGeO_4

Bond	Distance (Å)	Bond	Distance (Å)
Li(1)–O(1)	1.80	Co–O(1)	1.87
Li(1)–O(2)	2.12	Co–O(2)	1.83
Li(1)–O(3)	2.19	Co–O(3)	1.85
Li(1)–O(4)	1.66	Co–O(4)	1.91
<m>	**1.94**	<m>	**1.86**
Li(2)–O(1)	2.19	Ge–O(1)	1.89
Li(2)–O(2)	2.25	Ge–O(2)	1.80
Li(2)–O(3)	1.97	Ge–O(3)	1.82
Li(2)–O(4)	1.80	Ge–O(4)	1.89
<m>	**2.05**	<m>	**1.85**

Bond	Angle (°)	Bond	Angle (°)
O(1)–Co–O(3)	106.46	O(2)–Ge–O(3)	102.51
O(1)–Co–O(2)	110.86	O(2)–Ge–O(4)	110.72
O(1)–Co–O(4)	114.59	O(2)–Ge–O(1)	111.83
O(3)–Co–O(2)	112.84	O(3)–Ge–O(4)	103.80
O(3)–Co–O(4)	110.16	O(3)–Ge–O(1)	115.96
O(2)–Co–O(4)	102.09	O(4)–Ge–O(1)	111.44
<O–Co–O>	**109.50**	<O–Ge–O>	**109.37**

covalently connected to the BO_4 polyhedra.[17] The Pn-Li_2CoGeO_4 structure can be viewed as an accumulation of infinite zig–zag elements alternating $(CoO_4)^{4-}$ and $(GeO_4)^{4-}$ in the (a, b) plan.

These tetrahedra built up a network with channels along the c axis in which the Li^+ ions have conducting pathways as showed in the Fig. 2. In the repetitive structure moiety, the CoO_4 and GeO_4 tetrahedra pointed into (100), whereas the other moiety pointed into the inverse direction (−100) in an alternate way and were connected only by sharing corners. The process was generated by the parallel movement of Li^+-ions along the c axis. It consists of binary chains of distorted $(CoO_4)^{4-}$ tetrahedra that were alongside-propagated in the (a, b) plan and interlinked partially by corner-sharing. Each $(GeO_4)^4$ group was thus encircled by four $(CoO_4)^4$ tetrahedra and inversely, eventually forming cavities. The average values of the bond lengths of Co–O and Ge–O in the $(CoO_4)^4$ and $(GeO_4)^4$ tetrahedra are 1.86 Å and 1.85 Å respectively and are presented in the Table 3. It is very significant to point out that Li (1) and Li (2) were confined in two opposite direction cavities (T1 and T2) (Fig. 2). This result would have an important influence on the migration process of Li^+-ions.

3.3. Morphological description and particle size distribution studied by SEM and TEM imaging

The SEM and EDX technique were used in order to study the composition and the morphology of our sample.[18] These supplementary studies make it feasible to differentiate the elements presents in the studied compound by detecting backscattered electrons. Based on the Fig. 3(a), it is clear that this micrograph show a collection of small and large-sized grains homogeneously distributed everywhere into the compound. Furthermore, there is a tendency to shape some types of agglomeration, due to the humidity caused by lithium attendance. In fact, as shown in the Fig. 3(b), the EDX spectrum reveals the presence of different elements, oxygen, cobalt and germanium. It is interesting to observe that lithium is not present in the Fig. 3(b) since it has the same atomic number than the element used as a reference for this compound which is beryllium. In order to further estimate the particle size distribution, the transmission electron microscopy (TEM) analysis was performed and the result is represented in the
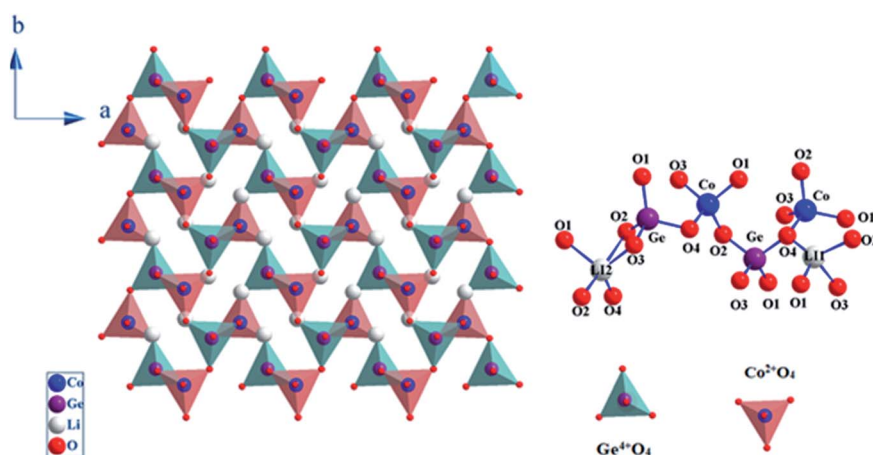

Fig. 2 Li_2CoGeO_4 structures as a 'Wurtzite' with corner sharing CoO_4 tetrahedra linked *via* GeO_4 tetrahedra.
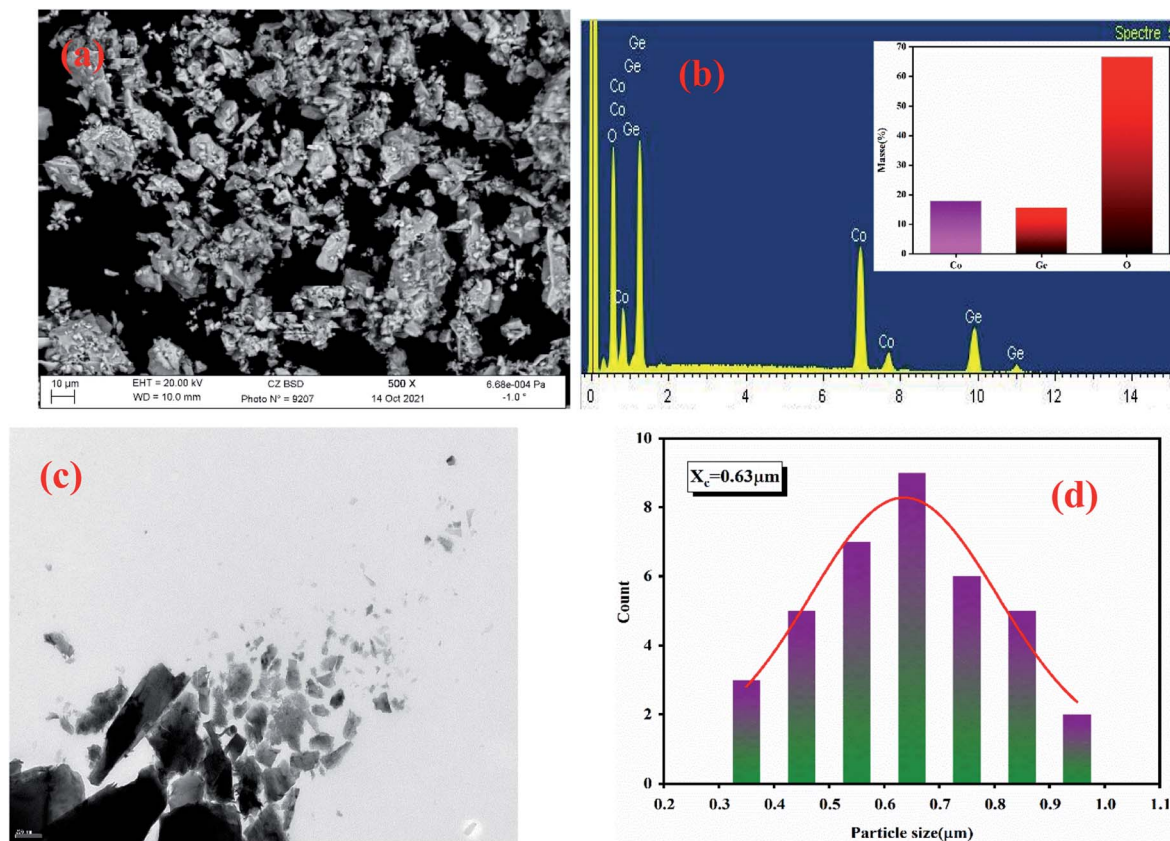
Fig. 3 SEM image of LCG (a), the elemental analysis by EDX (b), TEM image of LCG (c) and the particle size distribution of LCG (d).

Fig. 3(c). By using the Image J software a manual statistical count of grain size was affected on TEM images. The results are shown as histograms in the Fig. 3(d) as counts (grain number) *versus* particle sizes. The figure shows that the gained particles sizes are mostly in the order of 0.4–0.9 μm.

3.4. Infrared spectra

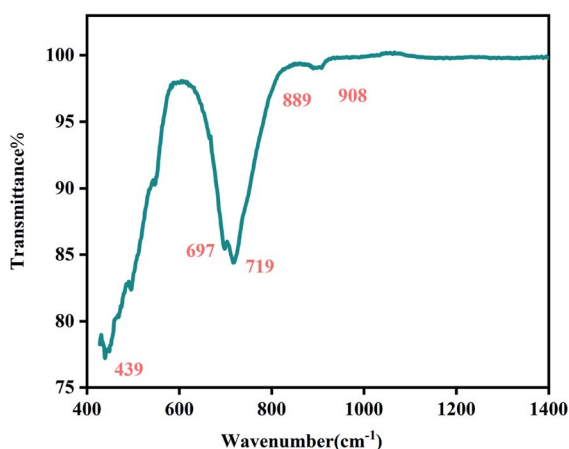The Fig. 4 shows the FTIR spectrum of the Li_2CoGeO_4 compound acquired at room temperature and in the

Fig. 4 FTIR spectrum of Li_2CoGeO_4 at room temperature.

wavenumber range from 400 cm^{-1} to 4000 cm^{-1}. Based on spectra of comparable compounds, a detailed attribution of the bands is able to be performed.[19–21] The band is centered at 439 cm^{-1} and corresponds to the asymmetric binding frequencies of GeO_4. The remaining characteristic bands higher than 600 cm^{-1} are relative to the antisymmetric stretching GeO_4.

3.5. Optical properties

3.5.1 Absorbance spectra. In order to understand the effect of the CoO_4 tetrahedron on electronic structures, a study of optical properties becomes useful. The Fig. 5(a) displays the room temperature absorbance spectra of the LCG compound in the wavelength range from 200 to 800 nm. The resulting spectra show the lowest energy absorption peak in the UV region at 286 nm. Based on bibliographic studies,[22,23] it is possible to discover three types of transitions from ground state $^4A_{2g}$ for Co^{2+} ions in tetrahedral coordination: $^4A_{2g}$–$^4T_{2g}$ (ν_1), $^4A_{2g}$–$^4T_{1g}$(F) (ν_2), $^4A_{2g}$(F)–$^4T_{1g}$(P) (ν_3). The ν_1 and ν_2 transitions arise in the low-frequency region (below than 10.000 cm^{-1}) for the oxygen ligands, which is not spotted by our UV-vis spectrometer. The $^4A_{2g}$(F)–$^4T_{1g}$(P) (ν_3) transition is detected at 584 nm, whose ^4F term is the ground atom term for a free Co^{2+} ion and ^4P is the first excited term. Besides, in the studied sample, the spectra contain two sub band absorption bands located at 530 and 665 nm. These peaks are linked to the d–d transitions of the tetrahedral-coordinated Co^{2+} ions. The two
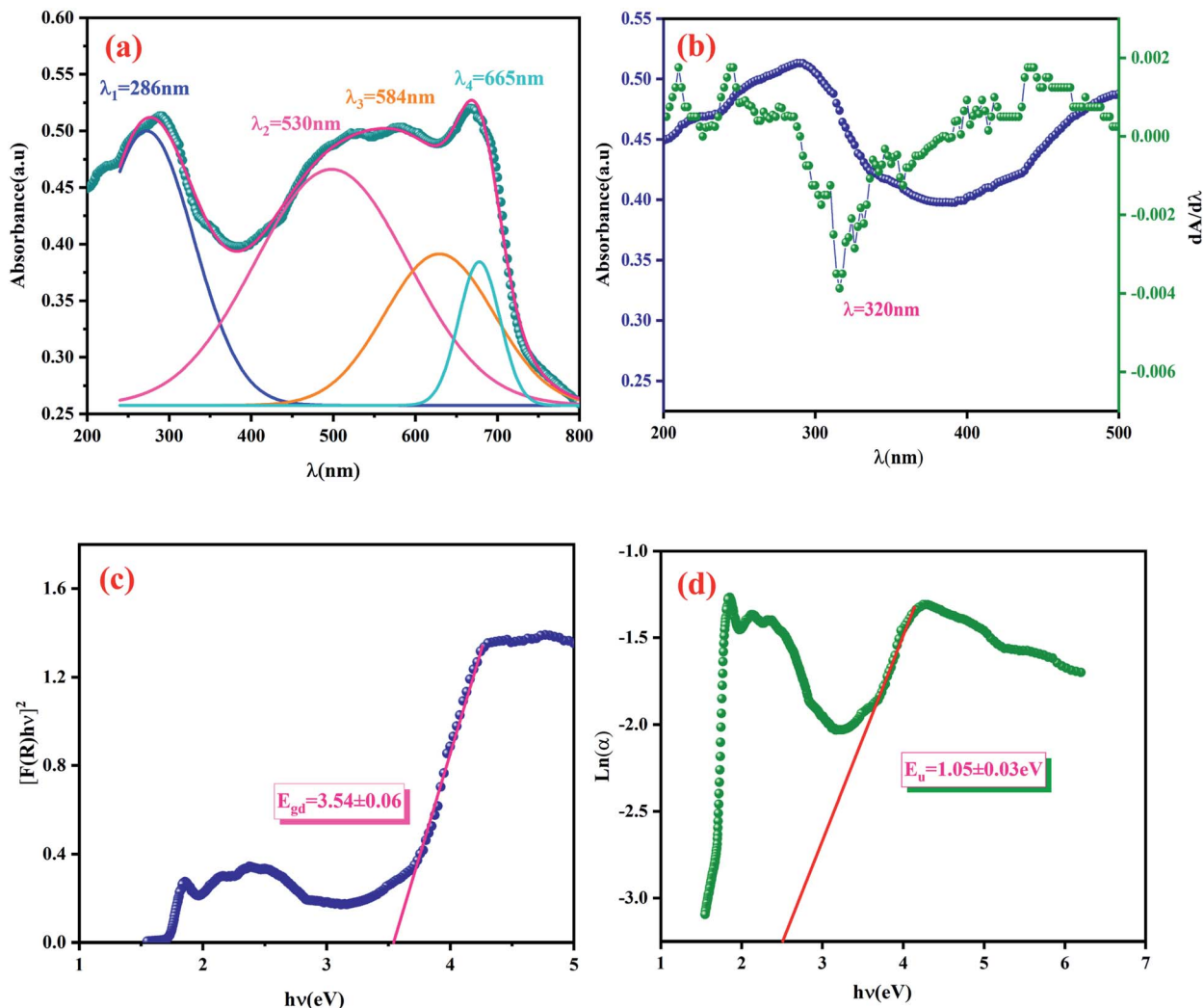
Fig. 5 Absorbance spectra of LCG measured at room temperature (a), evolution of dA/dλ and the absorbance A as a function of λ (b), plot of ($F(R)$ $h\nu$)^2 versus ($h\nu$) of LCG compound (c) and determination of the Urbach energy for the LCG compound (d).

absorption bands can be attributed to $^4A_2(F) \rightarrow$ $^2A_1(G)$ and $^4A_2(F) \rightarrow$ $^2E(G)$ field transitions, respectively.[24] Therefore, we conclude that the ground LCG sample contain Co^{2+} in the tetrahedral coordination.

3.5.2 Calculation of the optical band gap E_g. The band gap energy E_g of the sample can be determined directly from the minimum of the dA/dλ curve. In the Fig. 5(b), A and dA/dλ curves are plotted as a function of the wavelength λ. The band-gap E_g is estimated at 3.87 eV. The optical band gap of the compound was determined also according to the Kubelka–Munk and is given by the following equation:[25]

$$F(R) = \frac{(1-R)^2}{2R} \quad (2)$$

The dependence of $(F(R)h\nu)^2$ on the photon energy for the LCG compound is displayed in the Fig. 5(c). The straight-line extrapolation of these plots to the zero absorption spectrum gives the band gap energy $E_g = 3.54 \pm 0.06$ eV. Based on studies

of comparable compounds,[26] we can note that our compound has a lower gap energy value (3.54 eV).

3.5.3 Urbach energy. The disorder of the material has been characterized by the Urbach energy which corresponds to the transitions among the extended states of the valence band and the localized states of the conduction band.[27]

$$\alpha = \alpha_0 \exp\left(\frac{h\nu}{E_u}\right) \quad (3)$$

where E_u is the Urbach energy and α_0 is a constant. The Fig. 5(d) shows the photon – energy ($h\nu$) dependence of the Ln (α). The determinate value of Urbach energy is 0.96 eV.

3.6. Complex impedance analysis

3.6.1 Cole–Cole plots. The complex impedance spectroscopy technique (CSI) was used to investigate the electrical behavior of the material. It allows us to differentiate the real and imaginary constituents of the electrical parameters and allows a real image of the materials properties. The Fig. 6 displays the
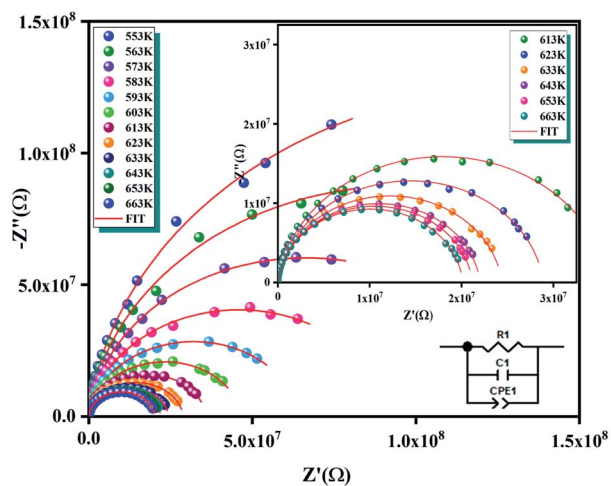
Fig. 6 The Nyquist plots for LCG at various temperatures.

Nyquist spectra (imaginary party of complex impedance $[Z''(\omega)]$) *versus* (real party of complex impedance $[Z'(\omega)]$) for Li_2CoGeO_4 compound at several temperatures [553 K to 663 K], which are characterized by the presence of semi-circular arcs. These semicircle arcs are most generally deformed and their centers placed below the Z' axis. This result means that the conduction of this compound does not follow the Debye formalism but obeys the Cole–Cole model. The appearance of a single half-circle indicates that electrical processes in the material arises basically due to the contribution from inner grains, which is expected from this compound where grain boundaries are produced because the powder was ground for 8 h.[28–30] We can note from these plots, that the radius of these semicircles decreases as the temperature increases, revealing the decrease in bulk resistance, and correspondingly the conduction mechanism is thermally activated. These graphs are fitted employing the Z-view software and the best adjustment is obtained when using an equivalent circuit. These spectra were successfully modeled by an equivalent circuit, including a parallel combination of resistances (R), capacitances (C) and fractal capacitances (CPE). The impedance of the fractal capacitance (CPE) is presented. The impedance has a constant phase angle in the complex plane. The CPE impedance is given by the following equation:[31]

$$Z_{CPE} = \frac{1}{(jQ\omega)^\alpha} \quad (4)$$

where, Q denotes the value of the capacitance of the element CPE, α the deviation degree with respect to the value of the pure capacitor. If α is equal to 0, the element behaves like an ohmic resistance independent of the frequency, if $\alpha = 1$, it is an ideal capacitor. The expressions of the real and imaginary constituents of the overall impedance were evaluated by the following equations:

$$Z' = \frac{R^{-1} + Q\omega^\alpha + \cos\left(\alpha\frac{\pi}{2}\right)}{\left(R^{-1} + Q\omega^\alpha \cos\left(\alpha\frac{\pi}{2}\right)\right)^2 + \left(C\omega + Q\omega^\alpha \sin\left(\alpha\frac{\pi}{2}\right)\right)^2} \quad (5)$$

$$-Z'' = \frac{C\omega + Q\omega^\alpha \sin\left(\alpha\frac{\pi}{2}\right)}{\left(R^{-1} + Q\omega^\alpha \cos\left(\alpha\frac{\pi}{2}\right)\right)^2 + \left(C\omega + Q\omega^\alpha \sin\left(\alpha\frac{\pi}{2}\right)\right)^2} \quad (6)$$

The Fig. 7(a) displays the frequency dependence of the real part of the impedance (Z') at different temperatures. The plots are described by an amplitude of Z' that decreases when the temperature and the frequency increase. This result leads to the possibility of a rise in the ac conductivity as a consequence of the diminution in the resistive behaviour of the material with an increase of the temperature.[32] Besides, all values of Z' merge at higher frequencies. This behaviour is an indication of the build-up of space charge polarization effect in the material at higher temperatures.[33,34] Furthermore, the Fig. 7(b) exhibits the frequency dependence of imaginary part of the impedance ($-Z''$) at various temperatures. We can note that the impedance plots are described by the existence of peaks ($-Z''_{max}$) at a particular frequency, which shift to higher frequencies with the rising temperature can be related to the type and intensity of the electrical relaxation phenomenon in the system. A important broadening of the peaks with an increase of temperatures suggests the existence of a temperature-reliant relaxation process in the system. The asymmetric widening of the peaks suggests the existence of electrical processes in the system which enlarges the relaxation time (marked by peak breadth) with two equilibrium portions. The relaxation types may probably be electrons/immobile species at low temperatures and defects at higher temperature.[35] Finally, at higher frequencies, Z'' reach a plateau for all temperatures, which may probably indicate an accumulation of space charges in the system.[36] In the following figures (Fig. 7(a) and (b)) we point out a good agreement between the experimental curve (scatter) and theoretical (line) data. This result shows that the proposed equivalent circuit characterises the behaviour of the studied sample.

3.6.2 D.C. conductivity. On the basis of the parameter values determined from the equivalent circuit using the Z-view software, the continuous conductivity of Li_2CoGeO_4 compound is calculated at every temperature with the following equation:[37]

$$\sigma_{dc} = \frac{e}{RS} \quad (7)$$

where e is the thickness of the compound, S the electrolyte–electrode contact area and R the bulk resistance value. The Fig. 8 displays the relaxation conductivity as a function of inverse temperature for Li_2CoGeO_4 sample. The activation energies of this process are estimated according to the Arrhenius law:

$$\sigma_{dc}T = A_0 \exp\left(\frac{E_a}{K_B T}\right) \quad (8)$$

where A_0 being the pre-exponential factor, E_a the activation energy and K_B the Boltzmann constant. From the plot, it is noticed the presence of two regions refereed as I ($T < 625$) and II ($T > 625$), linked with two activation energies disconnected by one temperatures $T = 625$ K. The observed change is probably due to the change in the conduction mechanism. This
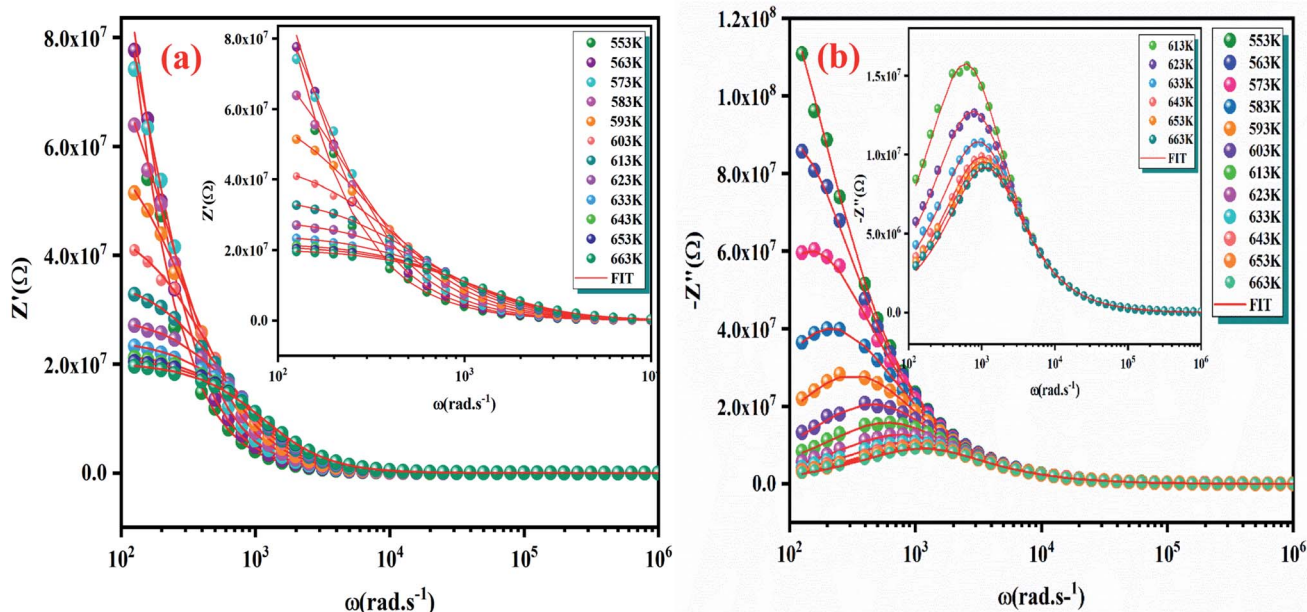
Fig. 7 Frequency dependence at different temperatures of real part Z' (a) and imaginary part Z'' (b) at various temperatures of Li_2CoGeO_4 compound.

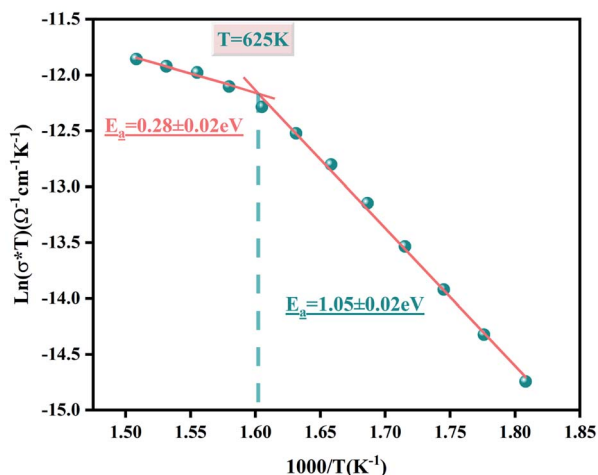Fig. 8 Arrhenius relation of Ln ($\sigma_{dc}T$) versus $1000/T$ for the Li_2CoGeO_4 compound.

behaviour is also observed in the literature for ceramic materials.[38] In both regions, the electrical conductivity increases linearly with temperature. This behaviour shows that σ_{dc} is a thermally activated transport process. The evaluated values of the activation energy are: $E_{aI} = 1.05 \pm 0.02$ eV and $E_{aII} = 0.28 \pm 0.02$ eV.

3.6.3 AC conductivity. In the goal to study the conduction mechanism in our material; the AC conductivity of the compound has been extensively studied. The frequency dependence of AC conductivity at various temperatures is presented in the Fig. 9. This phenomenon can be defined by the Jonscher's law:[39]

$$\sigma_{ac} = \sigma_{dc} + A\omega^s \qquad (9)$$

with σ_{dc} is the continuous conductivity, A a constant, $\omega = 2\pi f$ the angular frequency. The parameter s is the power exponent, which shows the degree of interaction between mobile ions and their surrounding networks ($0 < s < 1$). As it can be viewed, the conductivity plots reveal two regions at low- and high-frequencies. In the region I (at low frequencies), the AC conductivity is practically equivalent to the DC conductivity of the compound. Whereas in the region II (at high frequency region), σ_{ac} rises with increasing frequencies as well as temperature which is developed in semiconductor materials.

3.6.4 Conduction mechanism. In order to study the conduction mechanism within the Li_2CoGeO_4 compound,
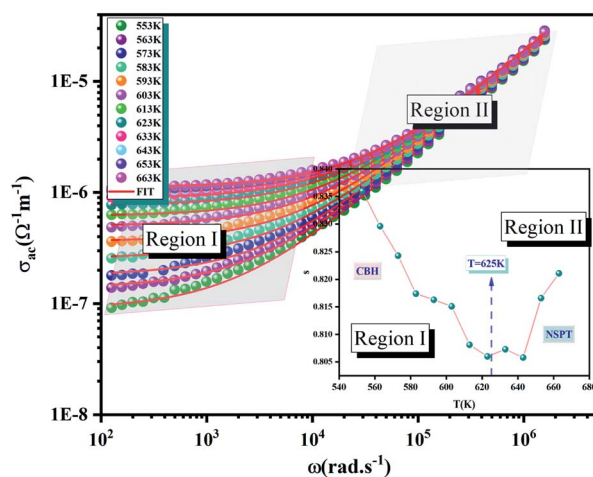

Fig. 9 The variation of the AC conductivity with the temperature as well as the frequency and the inset of the temperature dependence of the exponent s.

various theoretical models have been given in the literature such as:

- The correlated barrier hopping (CBH) model in which S decreases linearly with the rising temperature.[40,41]

- The small polaron tunneling (NSPT) model whither the exponent s rises with the increasing temperature.[42]

- The quantum mechanical tunneling (QMT) model is characterized by an exponent s which increases very slowly with temperature, practically equal to a value of 0.8.[43]

- The overlapping large polaron tunneling (OLPT) model submitted by Long.[44] The exponent s decreases with the temperatures to a minimum value and then increases slightly.

The Fig. 9 (inset) presents the temperature dependence of the exponent s. We can note that the exponent s exhibits two different regions as following:

- Part I, the exponent s decreases linearly with the temperature, which confirms that the (CBH) model is the suitable model.

- Part II, the exponent s increases with the increase in temperature to a minimum value and then increase with the temperature. Thus, the (NSPT) model is the appropriate model.

3.6.4.1 The correlated barrier hopping (CBH) model (region I).
This model was first enhanced by Pike for the single polaron jump and was thereafter developed by Eliott for the two-polaron jump.[45] Which considers the jump of Li$^+$ charge carriers amidst two sites on a barrier separating them? From the CBH formalism, the next equation gives the exponent s:[46]

$$s = 1 - \frac{6TK_B}{W_m - K_B T \ln\left(\frac{1}{\omega\tau}\right)} \tag{10}$$

where W_m is the binding energy of the carrier in its focused sites, K_B is the Boltzmann constant, and τ is a characteristic relaxation time is supposed to be 10^{-13} s. A very simple estimation of this equation gives the exponent (s):

$$s = 1 - \frac{6TK_B}{W_m} \tag{11}$$

For this simple model, the alternating conductivity is given by:[47]

$$\sigma_{ac} = \frac{n}{24}\pi^2 NNp\varepsilon' \omega R_\omega \tag{12}$$

with n is the number of polarons affected in the hopping process ($n = 1$ or 2), ε' is the dielectric constant of the compound. NNp is proportional to the square of the concentration of states and R_ω is the hopping distance for the condition ($\omega\tau = 1$) and it is given by:

$$R_\omega = \frac{4e^2}{\varepsilon'[W + KT \ln(\omega\tau)]} \tag{13}$$

Moreover, NNp can be presented by:

$$NNp = N_T^2 (\text{bipolaron-hoping})$$

$$NNp = N_T^2 \exp\left(\frac{-U_{eff}}{2K_B T}\right) \ (\text{single-polaron hopping})$$

The Fig. 10(a) displays the variation of the AC conductivity (Ln (σ_{ac})) as a function of ($1000/T$) in the sample Li$_2$CoGeO$_4$. The AC conductivity of this sample has been explained quite satisfactorily by considering a single conduction mechanism (single polaron). We can notice that theoretical values (lines) are in good agreement with the experimental values (symbols) and implied that this formalism is the simplest assumed formalism to qualify the approximate frequency dependence of AC conductivity. The different parameters used in the fitting procedure are summarized in Table 4. The negative sign of effective energy is connected with the strong interaction
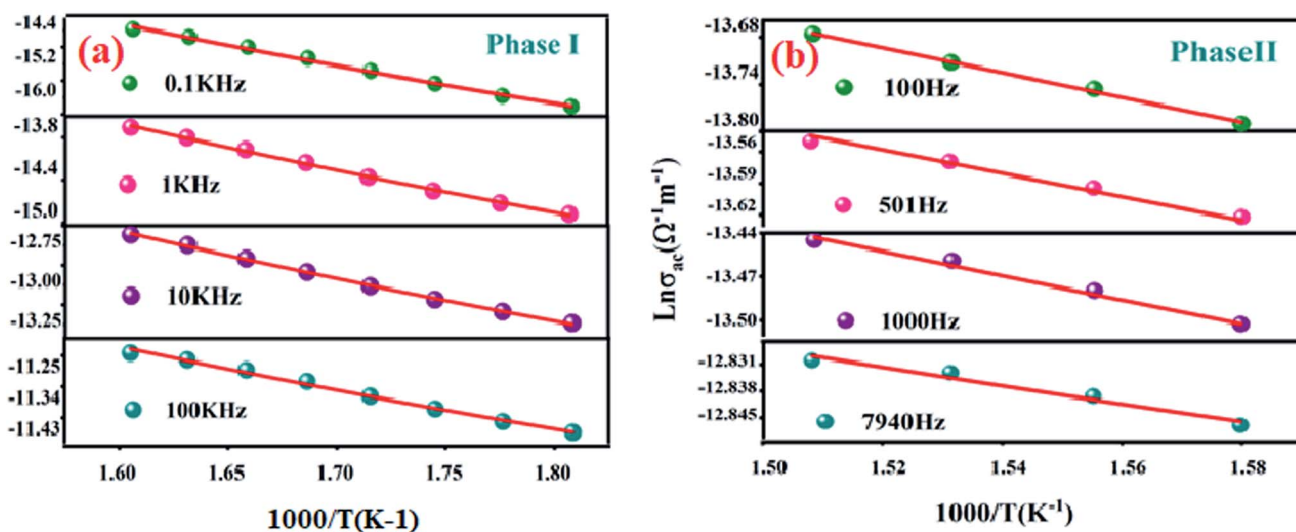

Fig. 10 Variation of Ln (σ_{ac}) with inverse of temperature at various frequencies for Li$_2$CoGeO$_4$ phase I (a) and phase II (b).

Table 4 Parameters used for the adjustment of the CBH model (I) and NSPT model (II)

Phase I				Phase II			
Frequency (Hz)	U_{eff} (eV)	$N(E_F)$ (eV^{-1} m^{-3})	W_m (eV)	Frequency (Hz)	$N(E_F)$ (eV^{-1} m^{-3})	α (Å^{-1})	W_m (eV)
1×10^2	-0.0046	9.58×10^{15}	0.3	1×10^2	5.61×10^{19}	1.18	0.34
1×10^3	-0.0031	1.83×10^{17}		501	2.99×10^{19}	1.3	0.19
1×10^4	-0.0014	5.84×10^{18}		1×10^3	2.14×10^{19}	1.35	0.07
1×10^5	-5.98×10^{-4}	5.65×10^{19}		7940	9.94×10^{18}	1.47	0.04

between electron and photon. The Fig. 11(a) shows the temperature dependence of R_ω at different frequencies. We note that the values of R_ω vary is in the interval of distances of 2.74–2.75 Å. These values are of the order of the inter-atomic distance Li–Li: 2.75 Å. Based on these results, it may be thought that the AC conductivity in Li$_2$CoGeO$_4$ is assured by the mobility of polarons because of the movement of Li$^+$ ions located in cavities along the c-axis.

3.6.4.2 The non-overlapping small-polaron tunnelling (NSPT) model (region II). In the NSPT formalism, the exponent s could be determined by the following equation:[48]

$$s = 1 + \frac{4K_B T}{W_m - K_B T \ln(\omega\tau_0)} \quad (14)$$

when $W_m/K_B T$ can take big values, the parameter is contracted to:

$$s = 1 + \frac{4K_B T}{W_m} \quad (15)$$

Considering the NSPT approach, σ_{ac} was given by the following formula:[49]

$$\sigma_{ac} = \frac{(\pi - e)^2 K_B T \alpha^{-1} \omega [N(E_F)]^2 R_\omega^4}{12} \quad (16)$$

where

$$R_\omega = \frac{1}{2\alpha}\left[\ln\left(\frac{1}{\omega\tau_0}\right) - \frac{W_m}{K_B T}\right] \quad (17)$$

α^{-1} represents the spatial extension of the polaron, R_ω the tunnelling distance, and $N(E_F)$ the density of states near the Fermi level. The Fig. 10(b) displays the evolution of the AC conductivity (Ln (σ_{ac})) as a function of (1000/T) at various frequencies in region II. We can observe that the theoretical calculations (lines) are in good agreement with the experimental data (symbol). The different parameters determined for this model are shown in the Table 4. Considering the results of adjustment, we represent in Fig. 11(b) the evolution of the tuning distance of R_ω as a function of the temperature. So, it is remarkable that R_ω increases with the increasing temperature. Consequently, in this model it is evident that the values of R_ω vary in the interval of distances of 1 Å to 3.5 Å. These values are in the same order of magnitude than the interatomic spacing Li–Li distances which was found to be 2.77 Å. From this observation we can conclude that the conduction process is assured by the mobility of small polarons because of the movement of Li$^+$ ions located in cavities along the [001] axis.

3.6.5 Electrical modulus analysis. The electrical modulus is given by:
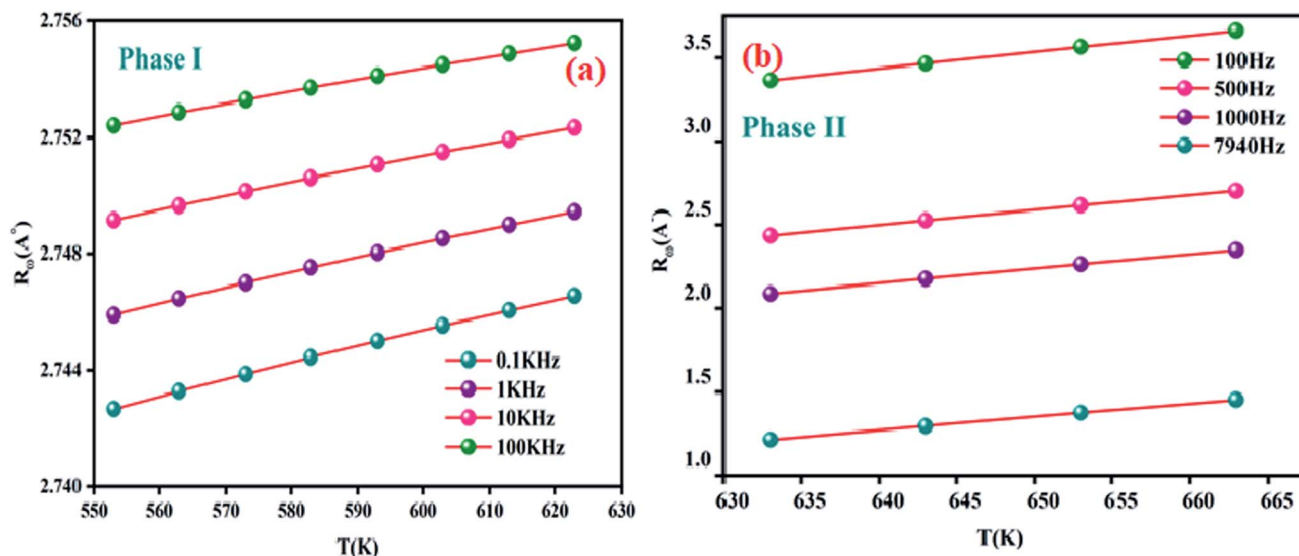

Fig. 11 Variation of the hopping tunneling distance R_ω as a function as temperature at different frequencies phase (I) (a) and phase (II) (b).
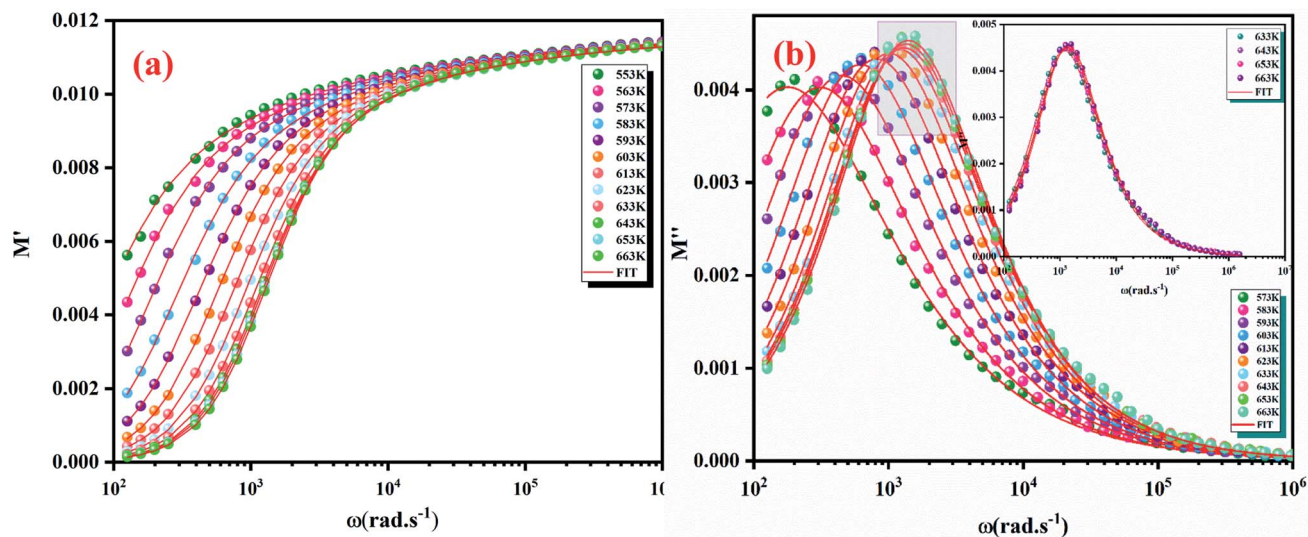
Fig. 12   Frequency dependence of real part (M') (a) and imaginary part (M'') of electric modulus at various temperatures (b).

$$M^* = M' + jM'' \tag{18}$$

$$M' = \omega C_0 Z'' \tag{19}$$

$$M'' = \omega C_0 Z' \tag{20}$$

where M', M'', Z' and Z'' are the real and imaginary parts of the complex modulus M^* and electric impedance Z^*, respectively. $C_0 = \varepsilon_0 S/e$ is the void capacitance of the measuring unit, S the electrolyte–electrode connect area, ε_0 is the permittivity of the open space, e the thickness of the compound and $\omega = 2\pi f$ with f being the frequency in Hz. The Fig. 12(a) shows the temperature and frequency dependent plots of the real part of the complex modulus (M') for the prepared Li_2CoGeO_4. It was observed that the values of M' is very low (approaching zero) at low frequency region. This can be due to the absence or low electrode polarization phenomenon.[50] Over and above that, it is noticeable a dispersion simultaneously with a frequency rise (supposedly

approaching M^∞). This result can be assigned to conduction phenomena due to the short range mobility of charge carriers.[51–53] At high frequency, M' displays a saturation value (the plateau part), implying that the electrical characteristics of the materials are frequency-independent. The variation of the imaginary part (M'') of the modulus as a function of frequency at various temperatures is exposed in the Fig. 12(b). We can note that the imaginary part of the modulus (M'') presents a single relaxation peak, focused at the dispersion domain of the real part of the modulus (M') related with the grain impact. It is clear that the relaxation of M'' peaks shifted to the higher frequencies with the rising temperature and the charge carrier movement becomes rapid, producing in a decrease in relaxation time.[54,55] This behaviour assumes that the relaxation is temperature dependent and that the charge carrier hopping is considered.[56,57] The spectra in this figure displays asymmetric and broad peaks suggesting that the conduction mechanism is
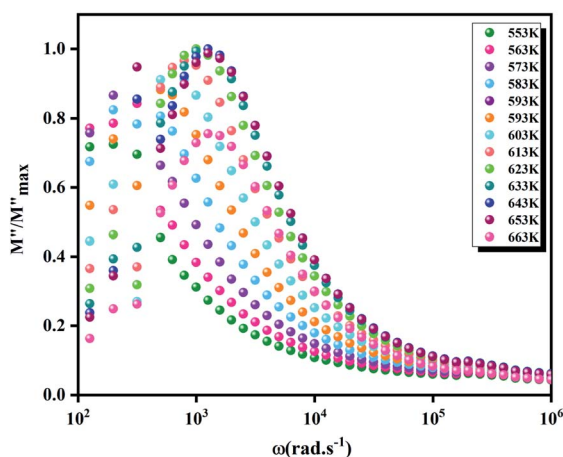

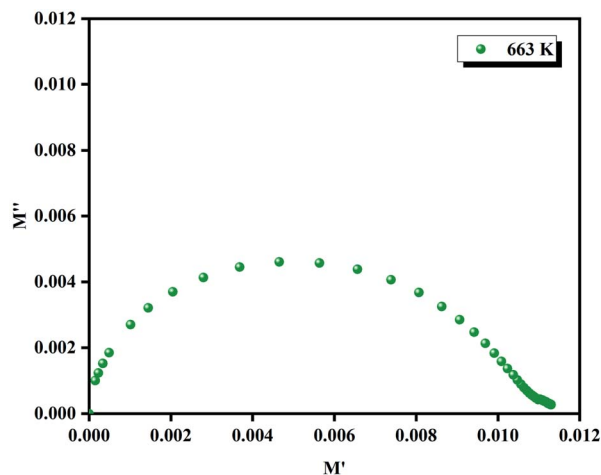Fig. 13   The normalized imaginary part of modulus M''/M''_{max}.

Fig. 14   Nyquist (M'' vs. M') plot at 663 K and the inset of the Ln (ω_{max}) as a function of the opposite of the absolute temperature (1000/T).

linked to non-Debye type.[58] The Fig. 13 represents the variation of M''/M''_{max} (the normalized imaginary part of the modulus) as a function of the frequency at various temperatures. The benefit of these plots is to demonstrate that the relaxation mechanism is dominated by the short or long distance movement of charge carriers. From the Fig. 13 it can be noted that the isolation between the normalized peaks M'' point out that the relaxation mechanism is controlled by the short distance displacement of the charge carriers. The Cole–Cole plot (M'' vs. M') for Li$_2$CoGeO$_4$ at $T = 663$ K is shown in the Fig. 14. The Cole–Cole plot (M'' vs. M') is more powerful than the Nyquist plot of impedance (Z'' vs. Z') in isolating the relaxation effects from grains and grain boundaries in our compound. It can be observed from the Fig. 14 the presence of single semicircle presenting the existence of electrical relaxation phenomena in our sample and also approves the only-phase characteristics of the studied material. For each temperature, the frequency ω_{max} designates the relaxation time $\tau\omega = 1$. In order to gain the activation energy demanded for the dielectric relaxation process, the corresponding curve of Ln (ω_{max}) as a function of the opposite of the absolute temperature ($1000/T$) is shown in the inset of the Fig. 14. This plot presents an Arrhenius-type behaviour defined by the next formula:[59]

$$\omega_{max} = \omega_0 \exp\left(\frac{E_a}{K_B T}\right) \tag{21}$$

The estimated values of the activation energy $(E_{\omega_{max}})$ are: $E_{aI} = 1.01 \pm 0.02$ eV and $E_{aII} = 0.25 \pm 0.02$ eV. It can be noted that the values of E_a evaluated from the conductivity are similar to the activation energy E_a determinate by modulus plots M'' implying that the electric parameters are accountable for the conduction and for the relaxation process and has the same impact in the investigated compound.

4.   Conclusions

In summary, the ceramic compound Li$_2$CoGeO$_4$ was prepared by a solid-state method and fritted at 1073 K. This sample was found to crystallize in the monoclinic system with *Pn* space group. The characterization by XRD verifies that the synthetized sample is purely monophasic without impurities belonging to the monoclinic *Pn* space group. The SEM images display the existence of particles with the same shape and irregular sizes. EDS spectra of Li$_2$CoGeO$_4$ confirm the presence of Li, Co, Ge, and O elements. Afterward the vibrational study by IR spectroscopy confirms the existence of the functional group $[GeO_4]^{4-}$. Moreover, the optical properties of Li$_2$CoGeO$_4$ samples are done in the UV-vis spectral domain for determining significant parameters such as the band gap energy (Urbach energy). Finally, the analysis of the Nyquist plots displays a non-Debye relaxation. The equivalent circuit is a (*R*//*C*//CPE). A unique electric contribution was detected in this material, which is explained with the migration of lithium ion. The survey of AC conductivity has been investigated in detail and designated on the basis of correlated barrier jump (CBH) model (region I) and non-overlapping small polaron tunnelling (NSPT) model in (region II). The study of these models (CBH and NSPT)

confirmed that the Li$^+$ ions ensured the alternative current conduction in Li$_2$CoGeO$_4$. The activation energy was calculated from the DC conductivity as well as modulus plots. The weak variations of the activation energy values suppose that the process has a similar relaxation behaviour and conduction mechanism.

Conflicts of interest

There are no conflicts of interest.

References

1   L. Xiukai, O. Shuxin, K. Naoki and Y. Jinhua, Novel Ag2ZnGeO4 photocatalyst for dye degradation under visible light irradiation, *Appl. Catal., A*, 2008, **334**, 51–58.

2   Z. Ning, O. Shuxin, K. Tetsuya and Y. Jinhua, Synthesis of hierarchical Ag2ZnGeO4 hollow spheres for enhanced photocatalytic property, *Chem. Commun.*, 2012, **48**, 9894–9896.

3   L. Jin and Z. Gaoke, Facile synthesis and enhanced visible-light photocatalytic activity of micro/nanostructuredAg2ZnGeO4 hollow spheres, *Mater. Sci. Eng.*, 2015, **193**, 198–205.

4   J. McDonald, Z. Ruigang, L. Chen, Z. Li Qin, Z. Ruibo, M. Stanley Whittingham and J. Hongfei, Hydrothermal synthesis, structure refinement, and electrochemical characterization of Li2CoGeO4 as an oxygen evolution catalyst, *J. Mater. Chem. A*, 2014, **2**, 8428–18434.

5   V. Nalbandyan, E. Zvereva, I. Shukaev, E. Gordon, V. Politaev, M. Whangbo, A. Petrenko, R. Denisov, M. Markina, M. Tzschoppe, K. Bukhteev, R. Klingeler and A. Vasiliev, A2MnXO4 family (A = Li, Na, Ag; X = Si, Ge): structural and magnetic properties, *Inorg. Chem.*, 2017, **56**, 14023–14039.

6   J. Grins, Structure and ionic conductivity of Na2BeGeO4, *J. Solid State Chem.*, 1995, **118**, 62–65.

7   J. Kamphorst and E. Hellstrom, Fast Li ionic conduction in solid solutions of the system Li4GeO4-Li2ZnGeO4-Li3PO4, *Solid State Ionics*, 1980, **1**, 187–197.

8   G. Vaivars, Synthesis, structure and conductivity of Ag2ZnSiO4, Ag2ZnGeO4 and Ag2BeSiO4, *Solid State Ionics*, 1995, **78**, 259–267.

9   S. Ben Yahya and B. Louati, Vibrational analysis and AC electrical conduction behavior of lithium zinc orthogermanate, *Ionics*, 2021, **27**, 3027–3034.

10 S. Ben yahya and B. Louati, Characterization of the structure and conduction behavior of overlapping polaron tunnel of dipotassium zinc orthogermanate, *J. Alloys Compd.*, 2021, **876**, 159972.

11 G. He, G. Popov and L. F. Nazar, Hydrothermal Synthesis and Electrochemical Properties of Li2CoSiO4/C Nano spheres, *Chem. Mater.*, 2013, **25**, 1024–1031.

12 G. Zhong, Y. Li, P. Yan, Z. Liu, M. Xie and H. Lin, Structural, Electronic, and Electrochemical Properties of Cathode Materials Li2MSiO4 (M = Mn, Fe, and Co): Density

Functional Calculations, *J. Phys. Chem. C*, 2010, **114**, 3693–3700.

13 C. Lyness, B. Delobel, A. R. Armstrong and P. G. Bruce, The lithium intercalation compounds Li2CoSiO4 and its behaviour as a positive electrode for lithium batteries, *Chem. Commun.*, 2007, **46**, 4890–4892.

14 A. R. Armstrong, C. Lyness, M. Ménétrier and P. G. Bruce, Structural Polymorphism in Li2CoSiO4 Intercalation Electrodes: A Combined Diffraction and NMR Study, *Chem. Mater.*, 2010, **22**, 1892–1900.

15 H. M. Rietveld, A profile refinement method for nuclear and magnetic structures, *J. Appl. Crystallogr.*, 1969, **2**, 65–71.

16 T. Roisnel and J. Rodriguez-Carvajal, EPDIC-8, European Powder Diffraction Conference, *Powder Diffr.*, 2002, **17**, 337–338.

17 V. Nalbandyan, E. Zvereva, I. Shukaev, E. Gordon, V. Politaev, M. Whangbo, A. Petrenko, R. Denisov, M. Markina, M. Tzschoppe, K. Bukhteev, R. Klingeler and A. Vasiliev, A2MnXO4 family (A = Li, Na, Ag; X = Si, Ge): structural and magnetic properties, *Inorg. Chem.*, 2017, **56**, 14023–14039.

18 M. Enneffati, B. Louati, K. Guidara, M. Rasheed and R. Barillé, Crystal structure characterization and AC electrical conduction behavior of sodium cadmium orthophosphate, *J. Mater. Sci.: Mater. Electron.*, 2018, **29**, 171–179.

19 N. L. Ross and A. Navrotsky, The Mg2GeO4 olivine-spinel phase transition, *Phys. Chem. Miner.*, 1987, **14**, 473–481.

20 H. L. Zheng, Z. C. Zhang, J. G. Zhou, S. S. Yang and J. Zhao, Vibrational spectra of CaGa2O4, Ca2GeO4, CaIn2O4 and CaSnO3 prepared by electrospinning, *Appl. Phys. A*, 2012, **108**, 465–473.

21 V. V. Fomichev and E. V. Proskuryakova, Vibrational spectra and energy characteristics of the superionics Li4SiO4 and Li4GeO4, *J. Solid State Chem.*, 1997, **134**, 232–237.

22 N. V. Kosova, V. F. Anufrienko, T. V. Larina, A. Rougier, L. Aymard and J. M. Tarasconz, Disordering and electronic state of cobalt ions in mechano chemically synthesized LiCoO2, *J. Solid State Chem.*, 2002, **165**, 56–64.

23 O. V. Livitska, N. Y. Strutynska, I. V. Zatovsky and N. S. Slobodyanik, The double phosphates MIMIIPO4 (MI = Na, K; MII = Mg, Mn, Co, Ni, Zn) – synthesis from chloride melts and characterization, *Cryst. Res. Technol.*, 2015, **50**, 626–632.

24 D. Senol, E. Ozugurlu and L. Arda, The effect of cobalt and boron on the structural, microstructural, and optoelectronic properties of ZnO nanoparticles, *Ceram. Int.*, 2020, **46**, 7033–7044.

25 P. Kubelka and F. Munk, An article on optics of paint layers, *J. Tech. Phys.*, 1931, **12**, 593.

26 Y. Jin, Y. Hu, Y. Fu, G. Ju, Z. Mu, R. Chen, J. Lin and Z. Wang, Preparation, Design, and Characterization of the Novel Long Persistent Phosphors: Na2 ZnGeO4 and Na2 ZnGeO4 :Mn2+, *J. Am. Ceram. Soc.*, 2015, **98**, 1555–1561.

27 A. Barhoumi, G. Leroy, B. Duponchel, J. Gest, L. Yang, N. Waldhoff and S. Guermazi, Aluminum doped ZnO thin films deposited by direct current sputtering: structural and optical properties, *Superlattices Microstruct.*, 2015, **82**, 483–498.

28 J. T. C. Irvine, D. C. Sinclair and A. R. West, Electroceramics: Characterization by Impedance Spectroscopy, *Adv. Mater.*, 1990, **2**, 132–138.

29 S. Selvasekarapandian and M. Vijaykumar, The ac impedance spectroscopy studies on LiDyO2, *Mater. Chem. Phys.*, 2003, **80**, 29–33.

30 S. Sen and R. N. P. Choudhary, Impedance studies of Sr modified BaZr0.05Ti0.95O3 ceramics, *Mater. Chem. Phys.*, 2004, **87**, 256–263.

31 A. K. Jonscher, the Interpretation of Non-Ideal Dielectric Admittance and Impedance Diagrams, *Phys. Status Solidi A*, 1975, **32**, 665–667.

32 P. C. Sati, M. Arora, S. Chauhan, M. Kumar and S. Chhoker, Structural, magnetic, vibrational and impedance properties of Pr and Ti codoped BiFeO3 multiferroic ceramics, *Ceram. Int.*, 2014, **40**, 7805–7816.

33 M. Ram, A.c. conductivity and dielectric properties of LiNi3/5Cu2/5VO4 ceramics, *Phys. B*, 2010, **405**, 1359–1361.

34 Y. Q. Lin, Y. J. Wu, X. M. Chen, S. P. Gu, J. Tong and S. Guan, Dielectric relaxation mechanisms of BiMn2O5 ceramics, *J. Appl. Phys.*, 2009, **105**, 054109.

35 S. Chatterjee, P. K. Mahapatra, R. N. P. Choudhary and A. K. Thakur, Complex impedance studies of sodium pyrotungstate–Na2W2O7, *Phys. Status Solidi A*, 2004, **201**, 588–595.

36 K. P. Chandra, K. Prasad and R. N. Gupta, Impedance spectroscopy study of an organic semiconductor: Alizarin, *Phys. B*, 2007, **388**, 118–123.

37 L. Mathes, T. Gigl, M. Leitner and C. Hugenschmidt, Breakdown of Arrhenius law of temperature-dependent vacancy concentration in FCC lanthanum, *Phys. Rev. B*, 2020, **101**, 134105.

38 A. Rahal, S. Megdiche Borchani, K. Guidara and M. Megdiche, Studies of electric, dielectric, and conduction mechanism of LiNiV0.5P0.5O4, *J. Alloys Compd.*, 2018, **735**, 1885–1892.

39 A. K. Jonscher, Analysis of the alternating current properties of ionic conductors, *J. Mater. Sci.*, 1978, **13**, 553–562.

40 S. R. Elliot, A.C. conduction in amorphous chalcogenide and pnictide semiconductors, *Adv. Phys.*, 1987, **36**, 135–217.

41 R. Punia, R. S. Kundu, M. Dult, S. Murugavel and N. Kishore, Temperature and frequency dependent conductivity of bismuth zinc vanadate semiconducting glassy system, *J. Appl. Phys.*, 2012, **112**, 083701–083705.

42 R. H. Chen, R. Y. Chang and S. C. Shern, Dielectric and AC ionic conductivity investigations in K3H(SeO4)2 single crystal, *J. Phys. Chem. Solids*, 2002, **63**, 2069–2077.

43 A. A. Dakhel, The annealing effect for structural, optical and electrical properties of dysprosium–manganese oxide films grown on Si substrate, *Solid-State Electron.*, 2005, **49**, 1996–2001.

44 A. R. Long, Frequency-dependent loss in amorphous semiconductors, *Adv. Phys.*, 1982, **31**, 553–637.

45 A. Zolanvari, N. Goyal and S. K. Tripathi, Electrical properties of a- GexSe100-x, *Pramana*, 2004, **63**, 617–625.

46 C. A. Hogarth, M. H. Islam and A. S. M. S. Rahman, D.c. and a.c. electrical properties of vacuum evaporated thin SiO/GeO2 films, *J. Mater. Sci.*, 1993, **28**, 518–528.

47 S. R. Elliott, A.c. conduction in amorphous chalcogenide and pnictide semiconductors, *Adv. Phys.*, 1987, **36**, 135–217.

48 M. D. Migahed, N. A. Bakr, M. I. Abdel-Hamid, O. El-Hanafy and M. El Nimr, Dielectric relaxation and electric modulus behavior in poly(vinyl alcohol)-based composite systems, *J. Appl. Polym. Sci.*, 1996, **59**, 655–662.

49 S. R. Elliot, *Adv. Phys.*, 1987, **36**, 135–217.

50 P. B. Macedo, C. T. Moynihan and R. Bose, *Phys. Chem. Glasses*, 1972, **13**, 171–179.

51 F. S. Howell, R. A. Bose, P. B. Macedo and C. T. Moynihan, Electrical relaxation in a glass- forming molten salt, *J. Phys. Chem.*, 1974, **78**, 639–648.

52 K. L. Nagi and C. Leon, Recent advances in relating macroscopic electrical relaxation data to microscopic movements of the ions in ionically conducting materials, *Solid State Ionics*, 1999, **125**, 81–90.

53 S. Sasaki, C. T. Prewitt and J. D. Bass, Orthorhombic perovskite CaTiO3 and CdTiO3: structure and space group, *Acta Crystallogr., Sect. C: Cryst. Struct. Commun.*, 1987, **43**, 1668–1674.

54 Y. Ben Taher, N. Moutia, A. Oueslati and M. Gargouri, Electrical properties, conduction mechanism and modulus of diphosphate compounds, *RSC Adv.*, 2016, **6**, 39750–39757.

55 R. Ranjan, R. Kumar, N. Kumar, B. Behera and R. N. P. Choudhary, Impedance and electric modulus analysis of Sm-modfied Pb(Zr0.55Ti0.45)1_x/4O3 ceramics, *J. Alloys Compd.*, 2011, **509**, 6388–6394.

56 F. Borsa, D. R. Torgeson, S. W. Martin and H. K. Patel, Relaxation and fluctuations in glassy fast-ion conductors: Wide-frequency-range NMR and conductivity measurements, *Phys. Rev. B: Condens. Matter Mater. Phys.*, 1992, **46**, 795–800.

57 A. Sinha and A. Dutta, Microstructure evolution, dielectric relaxation and scaling behavior of Dy-for-Fe substituted Ninanoferrites, *RSC Adv.*, 2015, **6**, 100330–100338.

58 A. Chen, Y. Zhi and L. E. Cross, Oxygen-vacancy-related low frequency dielectric relaxation and electrical conduction in Bi: SrTiO3, *Phys. Rev. B: Condens. Matter Mater. Phys.*, 2000, **62**, 228–236.

59 L. Liu, M. Wu, Y. Huang, Z. Yang, L. Fang and C. Hu, Frequency and temperature dependent dielectric and conductivity behavior of 0.95(K0.5Na0.5) NbO3-0.05BaTiO3 ceramic, *Mater. Chem. Phys.*, 2011, **126**, 769–772.